The development of cobalt phosphide co-catalysts on BiVO4 photoanodes to improve H2O2 production

Yuntao Xu, Yanfei Cao, Li Tan, Qiao Chen, Yuanxing Fang

Publication date
01-05-2023

Document Version
Accepted version

Published in
Journal of Colloid and Interface Science

Link to external publisher version
https://doi.org/10.1016/j.jcis.2022.11.120

The development of cobalt phosphide co-catalysts on $BiVO_4$ photoanodes to improve H_2O_2 production

Yuntao Xu, [1] Yanfei Cao, [1] Li Tan,[1*] Qiao Chen[2] and Yuanxing Fang[1*]

[1]State Key Laboratory of Photocatalysis on Energy and Environment, College of Chemistry, Fuzhou University, Fuzhou 350116, P. R. China

[2]Department of Chemistry, School of Life Sciences, University of Sussex, Brighton, BN1 9QJ, United Kingdom

Email: tan@fzu.edu.cn; yxfang@fzu.edu.cn.

Abstract

Photoanodic hydrogen peroxide (H_2O_2) production via water oxidation is limited by low yields and poor selectivity. Herein, four variations of cobalt phosphides, including pristine CoP and Co_2P crystals, and two mixed-phase cobalt phosphides (CoP/Co_2P) with different ratios, were applied as co-catalysts on the $BiVO_4$ (BVO) photoanode to improve H_2O_2 production. The optimal yield and selectivity were approximately 9.6 $\mu mol \cdot h^{-1} \cdot cm^{-2}$ and 25.2% at a voltage bias of 1.7 V vs. reversible hydrogen electrode (V_{RHE}) under sunlight illumination, respectively. This performance is ~1.8 times that of pristine BVO photoanode. The roles of the Co and P sites were investigated. In particular, the Co site promotes the breaking of one H-O bond in water to form $OH^{\bullet}$ radicals, which is the rate-determining step in H_2O_2 production. The P site plays an important role in the desorption of H_2O_2 formed from the catalyst, which is responsible for the recovery of fresh catalytic sites. Among the four samples, Co_2P exhibited the best performance for H_2O_2 production because it had the highest rate of $OH^{\bullet}$ formation owing to its improved accumulation property. This study offers a rational design strategy for co-catalysts for photoanodic H_2O_2 production.

Keywords: Hydrogen Peroxide; Cobalt phosphide; Photoanode; Water Oxidation; $BiVO_4$

1. Introduction

Hydrogen peroxide (H_2O_2) is an important chemical for the synthesis of basic commodities [1-3]. H_2O_2 is currently produced using the anthraquinone method, which involves the catalytic reduction and oxidation of anthraquinone, thus making its synthesis hazardous and expensive. H_2O_2 can be produced via photocatalytic reduction reaction [4-6] and water oxidation reactions. Photoanodic water oxidation reactions have attracted significant interest because they convert water to H_2O_2 using solar energy [7, 8]. This reaction is a two-electron process driven by a thermodynamic energy of 354 kJ/mol, corresponding to 1.76 V vs. reversible hydrogen electrode (V_{RHE}) [9, 10]. The main obstacle to this photoanodic reaction is the selective production of H_2O_2 because the reaction competes with the oxygen evolution reaction (OER) [11-14]. Although OER is a four-electron process, the required thermodynamic energy is only 237 kJ/mol [15-17], corresponding to 1.23 V_{RHE}, which is considerably lower than that for the H_2O_2 production [18-20].

Selectivity is therefore the main issue in the production of H_2O_2 via the water oxidation reaction, which is highly correlated with the co-catalyst or electrocatalyst at the surface of the photoanode [21-23]. In the past year, crystals containing Co or P have been investigated as co-catalysts to improve photoanodic water oxidation reactions for H_2O_2 production, including Co_3O_4 [21], Co^{2+} ions [24], and PO_4^{3+} ions [24], and many others [25, 26]. However, in-depth studies are required to understand the roles of the Co and P species in this reaction. Hence, cobalt phosphides (CoP/Co_2P) are an ideal model for this study. For the electrochemical water oxidation reaction, the transition

metal can act as an energy reservoir and active site for the rapid cleavage of an H-O bond in water to form an $OH^{\bullet}$ radical by shifting the valence state [19, 27, 28]. CoP crystals typically involve Co^{3+} ions; thus, the redox couple of Co^{3+}/Co^{4+} can form during the reaction. In comparison, Co_2P crystals contain Co^{1+} and Co^{2+} ions, resulting in the formation of a series of redox couples from Co^{1+} to Co^{4+}, including Co^{1+}/Co^{2+}, Co^{2+}/Co^{3+}, and Co^{3+}/Co^{4+}. The formation of the redox couple further promoted the formation of active intermediates, such as $OH^{\bullet}$ radicals, during the water oxidation reaction. This radical species may act as an intermediate for both H_2O_2 and O_2 formation. Hence, it is necessary to study the competition between the pathways of O_2 and H_2O_2 formation. Notably, the P sites are effective for the desorption of the produced H_2O_2 but not for O_2 [29, 30]. Therefore, by introducing both Co and P, the overall production of H_2O_2 can potentially increase.

In this study, pristine CoP and Co_2P crystals and mixed-phase cobalt phosphide (CoP/Co_2P) crystals were synthesized and used as co-catalysts to load onto the surface of $BiVO_4$ (BVO) photoanodes to improve H_2O_2 production. As a result, the optimal yield and selectivity were 9.6 $\mu mol \cdot h^{-1} \cdot cm^{-2}$ and 25.2%, respectively, at a voltage bias of 1.7 V_{RHE} under sunlight illumination. This performance is 1.8 times that of pristine BVO photoanode. The individual roles of the Co and P sites were investigated. The Co site is effective in breaking the H-O bond in water to form $OH^{\bullet}$, whereas the P site accelerates the desorption of the formed H_2O_2. As a co-catalyst on the BVO photoanode, Co_2P exhibited the optimal performance for H_2O_2 production owing to the highest rate of $OH^{\bullet}$ formation due to the improved photoexcited charge accumulation.

This study reports the role of a cobalt phosphide co-catalyst in enhanced photoanodic H_2O_2 production.

2. Experimental and Methods

2.1 Synthesis of $BiVO_4$ photoanodes

BVO films were prepared on fluorine-doped tin oxide (FTO, 10 mm × 25 mm, sheet resistance: 7 Ω/□, Wuhan Jingge Solar Energy Technology Co., Ltd) glass via electrochemical deposition [31]. In detail, $Bi(NO_3)_3 \cdot 5H_2O$ (0.97 g, 99 %, Sinopharm Chemical Reagent) was dissolved in HNO_3 solution (50 mL, pH = 1.7, 99 %, Sinopharm Chemical Reagent) to form a 0.04 M $Bi(NO_3)_3$ solution, and KI (3.32 g, 99 %, Thermo Scientific) was added to the solution. This solution was then mixed with absolute ethanol (20 mL, 99 %, Sinopharm Chemical Reagent) that containing 0.5 g p-benzoquinone (98%, Alfa Aesar). Subsequently, a typical three-electrode cell was used to electrodeposit the BiOI films on the FTO glass. Typically, an FTO glass, Ag/AgCl electrode, and platinum sheet were applied as the working, reference, and counter electrodes, respectively. The deposition was performed at -0.1 V vs. Ag/AgCl for 3 min. Subsequently, dimethyl sulfoxide solution (DMSO, 180 μL, 99 %, Sinopharm Chemical Reagent) containing 0.2 M vanadyl acetylacetonate ($C_{10}H_{14}O_5V$, 98 %, Aladdin) was dropped onto the BiOI electrode. The as-prepared electrode was thermally treated in a muffle furnace at 450 °C for 2 h to prepare BVO.

2.2 Loading cobalt phosphide on $BiVO_4$ photoanode

Pristine CoP and Co_2P crystal powder and diphase cobalt phosphide (CoP/Co_2P) crystal powders were synthesized using a hydrothermal approach [32]. $Co(NO_3)_2 \cdot 6H_2O$

(1.5 mmol, 99 %, Sinopharm Chemical Reagent), NH_4F (7.5 mmol, 96 %, Sinopharm Chemical Reagent), and $CO(NH_2)_2$ (99 %, Sinopharm Chemical Reagent) were dissolved in deionized water (15 mL). The solution was subsequently transferred into a 20 mL Teflon-lined stainless-steel autoclave and maintained at 120 °C for 6 h. Co(OH)F powder was collected and dried under vacuum at 70 °C for 10 h. Co(OH)F is the precursor of cobalt phosphides and Co_3O_4. Co_3O_4 was obtained by oxidizing Co(OH)F at 450 °C for 2 h. $NaH_2PO_2 \cdot H_2O$ (99 %, Sinopharm Chemical Reagent) and Co_3O_4 powders were mixed in the molar ratios of 5:1 and 3:1 and annealed at 350 °C in N_2 atmosphere for 4 h to obtain the diphase cobalt phosphides. To prepare pristine CoP and Co_2P crystals, NaH_2PO_2 and Co(OH)F powder were mixed in ratios of 6:1 and 2:1, respectively, and annealed at 350 °C in N_2 atmosphere for 4 h. The as-prepared cobalt phosphides were suspended and drop-coated on the BVO photoanodes as co-catalysts at a concentration of 3 μg/cm^2.

2.3 Characterizations

The structure and morphology of the cobalt phosphides and BVO based photoanodes were studied by a scanning electron microscope (SEM, SU8010, Hitachi). The crystallinity of cobalt phosphides and BVO based photoanodes was studied by a powder X-ray diffractometer (XRD, MiniFlex 600, Rigaku). High-resolution transmission electron microscopy (HRTEM, FEI Talos) with a FEI super-X energy dispersive spectroscopy (EDS) was performed to investigate the chemical composition of the photoanodes. The elemental composition and valence states of the catalysts were characterized by an X-ray photoelectron spectroscopy (XPS, ESCALB 250,

Thermofisher Scientific). The spectra were fitted by the Gauss-Lorentz function with the Sherry function after removing the background signal. The C 1s binding energy of 284.8 eV was used as the reference. The UPS data was collected by Thermo Fischer, ESCALAB 250Xi with He-lα source. The wavelength of the ultraviolet is 58.13 nm and the kinetic energy (*hv*) is 21.22 eV. It was used to determine the Fermi level and conduction band of the samples. A UV-Vis-NIR spectrophotometer (Cary 500, Varian) with a small integrating sphere was used to measure the diffuse reflection absorption of the films. The probability of charge recombination was measured using photoluminescence (PL) spectroscopy (F-7000, Hitachi). The colorimetric data was measured in a UV-Vis spectrophotometer (UH5300, Hitachi). The radical components were monitored by an electron paramagnetic resonance (EPR) spectrometer (A300 ESR, Bruker). Typically, 0.6 mg of the catalyst powder was suspended in 0.5 mL $KHCO_3$ solution (1.0 M). The evolution of the $OH^{\bullet}$ radicals under light illumination was measured by adding 5 μL of 5,5-dimethyl-1-pyrroline N-oxide (DMPO) to form DMPO-•OH adduct.

2.4 Photoelectrochemical production of H_2O_2

Photoelectrochemical (PEC) experiments were conducted using a three-electrode system. BVO-based photoanodes were used as the photoanode, and a KCl-saturated Ag/AgCl electrode and Pt foil were used as the reference and counter electrodes, respectively. An electrochemical workstation was used to study the PEC performance. A calibrated solar simulator with an AM 1.5 G filter was used as the light source. The experiment was performed in an electrochemical cell with two chambers separated by

a Nafion membrane. The electrolyte solutions for the working and counter electrodes were 1.0 M $KHCO_3$ and 0.2 M Na_2SO_4 [33], respectively. In this PEC system, a 1.0 $KHCO_3$ electrolyte solution was used to promote H_2O_2 formation, but this alkaline solution may lead to a large overpotential for H_2 evolution, possibly affecting H_2O_2 production. Therefore, a neutral solution was applied to the cathode to minimize the negative effects. Photoanodic H_2O_2 production was achieved with a voltage bias of 1.7 V_{RHE} and AM 1.5 G. Cyclic voltammetry (CV) was studied at 0.1–1.9 V_{RHE} and a scan speed of 5 mV/s [34]. There were three repeated cycles. CoP, Co_2P, and two mixed-phase cobalt phosphide materials were drop-coated onto the FTO substrate as photoelectrodes. Nyquist plots were acquired from the electrochemical impedance spectroscopy (EIS) measurements with modulation in the frequency range of 200 kHz to 100 mHz and illumination on or off at 1.7 V_{RHE}. The PEC decomposition of H_2O_2 was investigated on BVO, Co_3O_4-BVO, and CPB photoanodes under AM 1.5 G illumination; 1.0 M potassium borate solution with 1 mM H_2O_2 was used as the electrolyte. The electrolyte was extracted every 20 min to determine the resulting concentration of H_2O_2.

The quantity of H_2O_2 was determined using the Fe^{2+} colorimetric method based on Eq. 1 [35, 36]:

$$Fe^{2+} + H_2O_2 \rightarrow Fe^{3+} + 2OH^- \quad \text{(Eq. 1)}$$

In particular, HCl solution (3.0 M, 0.9 mL) was added to the of electrolyte solution (1.0 mL) containing the produced H_2O_2. Then, $FeSO_4 \cdot 7H_2O$ (0.2 mL, 0.1 M, 99%, Sinopharm Chemical Reagent) was added to the solution. The

concentration of produced H_2O_2 was determined using an ultraviolet–visible spectrophotometer.

EIS measurements were performed with and without illumination. The flat-band potentials of the materials were derived from the Mott–Schottky plots of EIS [37]. The selectivity (η) for H_2O_2 production was calculated using Eq. 2 [38]:

$$\eta\ (\%) = 2 \times N_{H_2O_2} \times 96485 / Q \times 100 \qquad \text{(Eq. 2)}$$

where $N_{H_2O_2}$ and Q denote the amount of produced H_2O_2 and total amount of charge involved in the reaction, respectively.

The incident photon-to-electron conversion efficiency (IPCE) for H_2O_2 production was determined under light irradiation at different wavelengths generated by a xenon lamp equipped with a monochromator. The IPEC was calculated using Eq. 3 [39]:

$$IPCE(\lambda) = (1240 \cdot j_P(\lambda)) / (\lambda \cdot E\lambda(\lambda)) \cdot \eta \qquad \text{(Eq. 3)}$$

where λ and $E\lambda(\lambda)$ are the wavelength and the incident light energy density at a certain wavelength, respectively, with the corresponding photocurrent density $j_P(\lambda)$. PEC studies were conducted in a three-electrode system, where the catalyst-coated FTO glass was used as the photoanode, where η is the selectivity for H_2O_2 production.

3. Results and discussion

3.1 Morphologies and chemical structures of cobalt phosphides

Pristine CoP and Co_2P nanoparticles and two mixed-phase CoP/Co_2P nanoparticles were synthesized using the hydrothermal method. The unit cells of CoP and Co_2P are shown in **Figure 1a**. The structure of CoP is clear, involving Co^{3+} and P^{3-} ions. Co_2P contained two inequivalent P^3 sites. In the first P^{3-} site, P^{3-} is bonded to three equivalent

Co^{2+} and six equivalent Co^{1+} atoms in a 9-coordinate geometry. In the second P^{3-} site, P^{3-} is bonded to three equivalent Co^{1+} and six equivalent Co^{2+} atoms in a 9-coordinate geometry. The X-ray diffraction (XRD) pattern in **Figure 1b** shows diffraction peaks from the CoP, Co_2P, and mixed-phase CoP/Co_2P nanoparticles. The peaks at 31.6°, 36.3°, 46.2°, 48.1°, 52.3°, and 56.8° corresponded to the (011), (111), (112), (103), and (301) crystal faces of CoP (JCPDS No. 00-029-0497), respectively, and the peaks located at 40.7°, 42.0°, and 52.0° were attributed to the (121), (220), and (230) crystal faces of Co_2P (JCPDS No. 01-070-8359). The samples with a mixed phase exhibited peaks from both CoP and Co_2P. Furthermore, based on the XRD results, the atomic ratio of Co to P was obtained, as shown in **Figure 1c**. The atomic ratios of Co:P in CoP and Co_2P were 1.11 and 1.90, respectively, which correlate with the stoichiometric ratios. Conversely, the mixed-phase cobalt phosphide samples had values of 1.34 and 1.78, indicating CoP contents of 66% and 22%, respectively.

The high-resolution X-ray photoelectron spectroscopy (XPS) spectra of Co 2p and P 2p from the different samples are shown in **Figures 1d** and **1e**, respectively. Owing to spin-orbit coupling, the Co 2p XPS spectra were formed with two bands assigned to Co $2p_{3/2}$ and Co $2p_{1/2}$. Each band can be deconvoluted into components associated with Co-P, Co-O, and satellite peaks. The binding energy of Co-P was lower than that of Co-O. As the Co:P ratio gradually decreased from Co_2P to CoP, the binding energy of Co-P increased, whereas the binding energy of the Co-O remained constant. In the P 2p XPS spectra, the peaks at 129.6 and 130.5 eV are assigned to the binding energies of P $2p_{3/2}$ and P $2p_{1/2}$ in Co-P, respectively, which shifted to higher binding energies with the

decrease in Co:P ratio. The behavior of the Co 2p and P 2p binding energies in Co-P suggests that Co_2P is relatively electron rich. The strong peak at 133.8 eV is assigned to the oxidized P. Both Co and P exhibit oxide peaks. The results show that the surfaces of the cobalt phosphides can be easily oxidized in the atmosphere. The XPS intensity of the surface oxides was exaggerated because XPS only collects photoelectrons within a thickness of 1–10 nm from the surface [40].

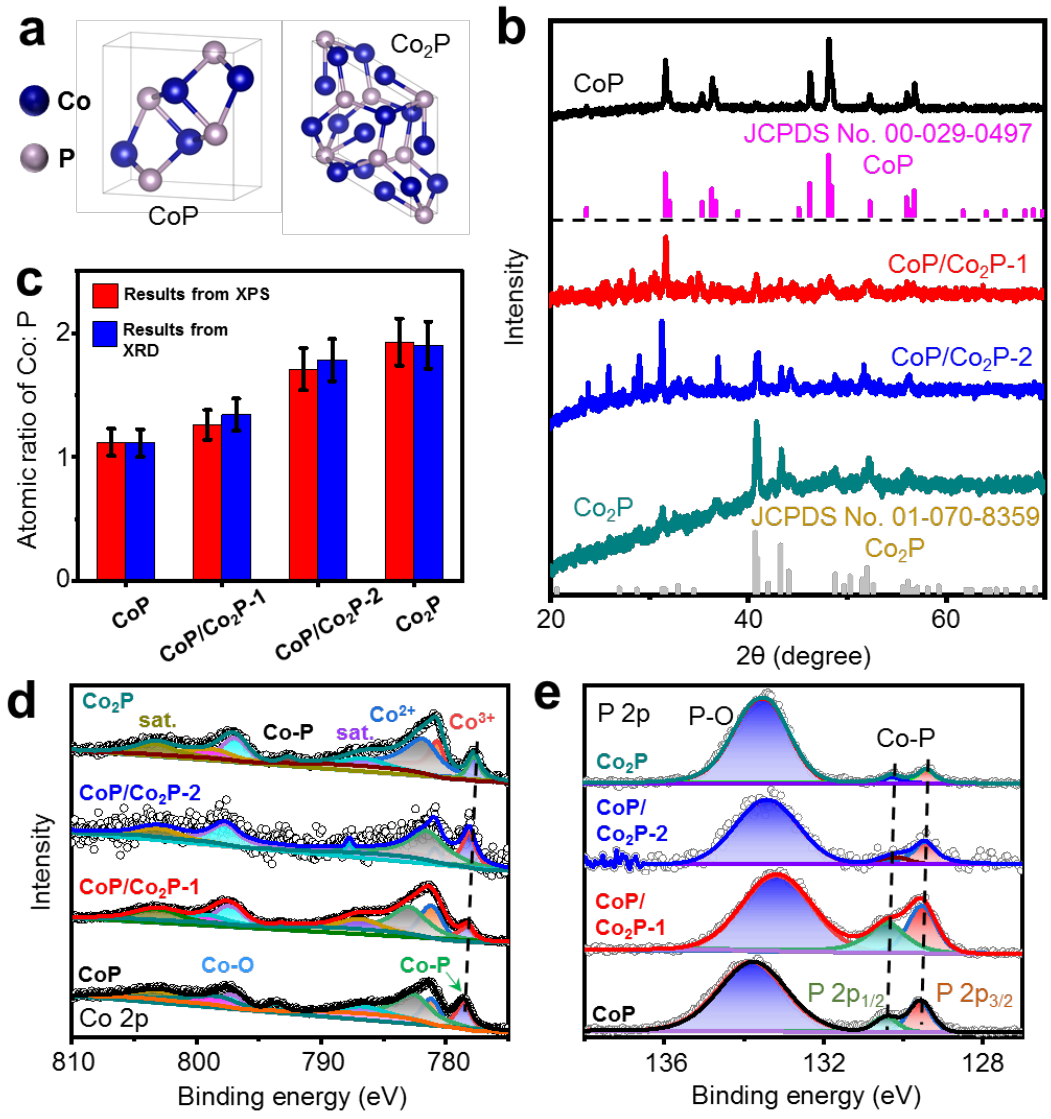

Figure 1. (a) The unit cells of CoP and Co_2P. (b) XRD spectra of CoP, CoP/Co_2P-1, CoP/Co_2P-2 and Co_2P (c) The atomic ratio of CoP, CoP/Co_2P-1, CoP/Co_2P-2, and Co_2P derivate from XRD and XPS spectra with twice independent data fitting and calculations, respectively. XPS spectra of (d) Co 2p and (e) P 2p of CoP, CoP/Co_2P-1,

CoP/Co_2P-2 and Co_2P.

Therefore, the atomic ratio of Co to P can be estimated from XPS (**Figure 1c**); this result generally agrees with the theoretical and XRD results [41]. CoP and Co_2P have Co:P ratios of 1.12 and 1.93, respectively, which correlate with the stoichiometric ratios. In addition, with the Co:P ratios of 1.26 and 1.71 for the CoP/Co_2P-1 and CoP/Co_2P-2 samples, the percentages of CoP in the composited material are 74% and 29%, respectively.

From the above results, the oxidation state of cobalt phosphides can be further investigated to gain a deeper understanding of the composition of cobalt phosphide materials. The oxidation states of Co and P are +0.7 and -0.7 for CoP, and +0.5 and -1.0 for Co_2P, respectively [42, 43]. Based on the Co:P ratios obtained above, the oxidation states of Co and P are +0.6 and -0.8 for CoP/Co_2P-1, and +0.5 and -0.9 for CoP/Co_2P-2, respectively.

In addition, the particle sizes of the cobalt phosphides were analyzed from the scanning electron microscopy (SEM) images (**Figure S1a to S1d**), yielding a mean size of ~20 nm, as shown in **Figure S1e**.

3.2 Loading cobalt phosphides on $BiVO_4$ photoanodes

The BVO photoanode was synthesized using an electrochemical deposition approach, and a highly porous structure was achieved, as shown in the Supporting Information. This porous structure was superior in overcoming the short minority diffusion length [44]. Cobalt phosphides (3.0 μg each) were spin-coated onto the BVO surface with an area of 1 cm^2. The CoP-, CoP/Co_2P-1-, CoP/Co_2P-2-, and Co_2P-loaded

photoanodes were labeled CPB-1, CPB-2, CPB-3, and CPB-4, respectively. The morphology and structure of the photoanodes were investigated by SEM. The top and cross-sectional views of the pristine BVO photoanode and CPB-4 are shown in **Figures 2a** to **2d**, and the other three samples are shown in **Figure S2**. An insignificant difference in the BVO morphology was observed after spin-coating the cobalt phosphide nanoparticles, possibly due to their nanoscale dimensions and the porous structure of BVO. A TEM study of the CPB-4 and BVO samples with elemental analysis is shown in **Figures 2f** to **2j**. Bi, O, V, Co, and P were homogeneously distributed, as shown in **Figures 2f** to **2j**, revealing the successful loading of cobalt phosphide particles. In addition, the high-resolution transmission electron microscopy images of the BVO, Co_2P, and CPB-4 photoanodes were obtained, as shown in **Figure 2k, 2l, and S3**. The (112) crystal plane of the BVO photoanode was observed (**Figure S3**) with a d-spacing of 3.08 Å. The crystal plane of Co_2P can be observed in **Figure 2k**, and 3.10 Å can be assigned to the (011) crystal plane. In addition, we can observe the Co_2P/BVO heterostructure in **Figure 2l** when Co_2P particles are loaded onto BVO.

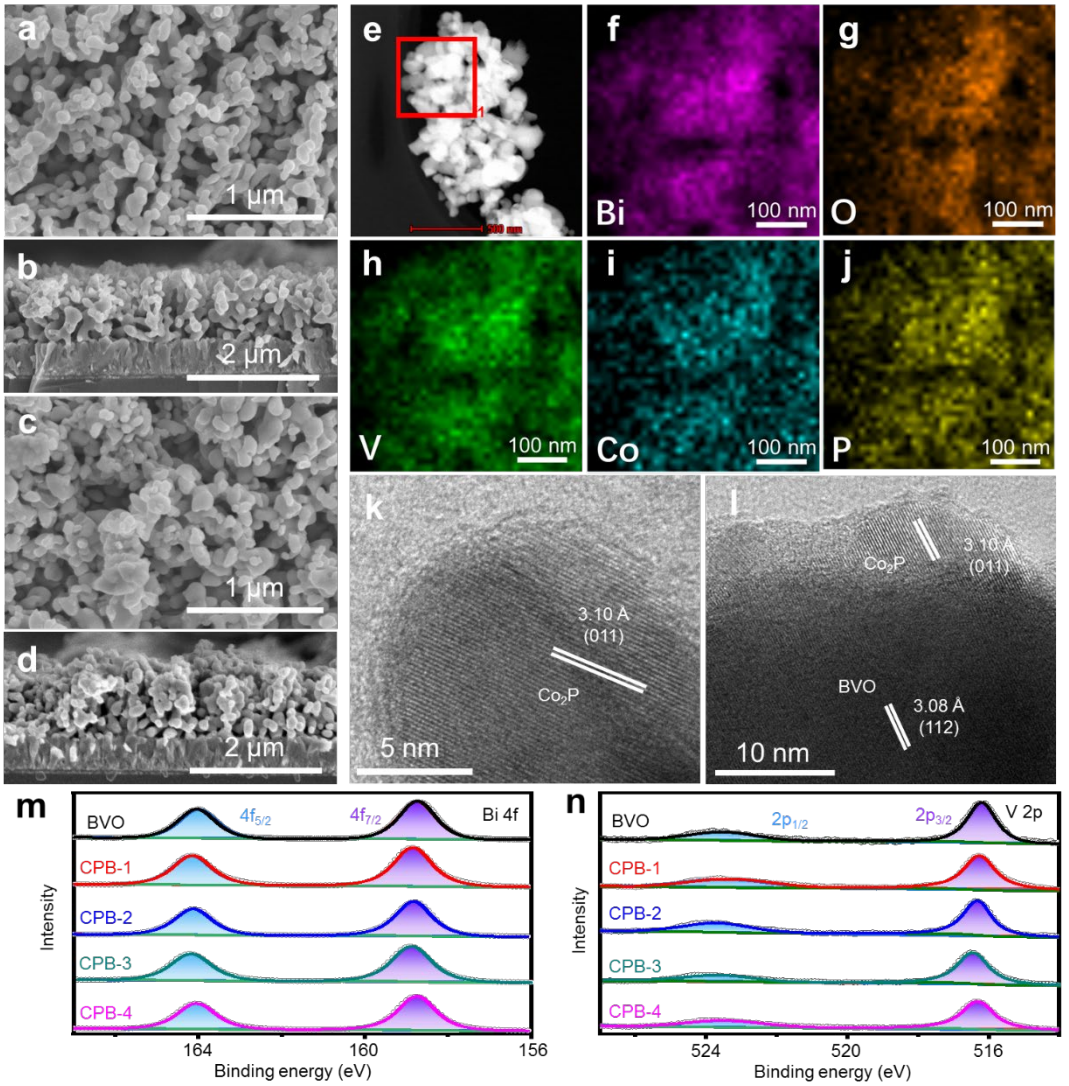

Figure 2. SEM images of the top and cross-sectional views of (a, b) BVO and (c, d) CPB-4. (e) High angle annular dark-field (HAADF) image of CPB-4. (f)-(j) The elements mapping of (f) Bi, (g) O, (h) V, (i) Co, and (j) P for CPB-4. HR-TEM images of (k) pristine BVO and (l) CPB-4 photoanode show typical crystal plane. High-resolution spectra of (m) Bi 4f and (n) V 2p for the BVO and CPB photoanodes.

XPS was used to investigate the modified BVO photoanode. The Bi 4f spectra in **Figure 2m** reveal two peaks at the binding energies of 158.8 and 164.1 eV, which are attributed to Bi $4f_{7/2}$ and Bi $4f_{5/2}$, respectively. The V 2p spectra in **Figure 2n** show two peaks at 516.2 and 523.6 eV, assigned to V $2p_{3/2}$ and V $2p_{1/2}$, respectively. In addition, both P 2p and Co 2p XPS spectra were acquired (**Figure S4**). However, owing to surface

oxidation, only peaks associated with the corresponding oxides were observed in the XPS spectra. The diffraction peak was also absent in the XRD spectra in **Figure S5** because of its low concentration and high dispersion.

3.3 H_2O_2 production by cobalt phosphide-modified BVO photoanodes

Photoanodic H_2O_2 production was performed using a standard three-electrode configuration in a 1.0 M $KHCO_3$ electrolyte solution under the illumination of a sunlight simulator (AM 1.5G). Linear sweep voltammetry (LSV) curves in **Figure 3a** were collected with an applied voltage bias scanning from 0 to 2.0 V_{RHE}. The photocurrent density increased with the loading of cobalt phosphides on the surface, and its value followed the order of BVO<CPB-1<CPB-2<CPB-3<CPB-4. Among them, the highest photocurrent density of 2.45 mA/cm^2 was achieved at 1.7 V_{RHE} from the CPB-4 sample, which is 1.7 times that of the pristine BVO photoanode. At 1.7 V_{RHE}, the concentration of the produced H_2O_2 was determined using the colorimetric method (**Figure S6**), with the corresponding H_2O_2 selectivity and yield presented in **Figures 3b** and **3c**, respectively [45]. The performance of H_2O_2 production in terms of both selectivity and yield followed the same order as the photocurrent density. The highest H_2O_2 production rate was achieved by CPB-4 (9.6 $\mu mol \cdot h^{-1} \cdot cm^{-2}$), which is approximately 1.8 times that of the pristine BVO photoanode (5.4 $\mu mol \cdot h^{-1} \cdot cm^{-2}$). Moreover, the best selectivity of 25% for H_2O_2 production was also realized by CPB-4, which was significantly improved relative to that of pristine BVO with a selectivity of 16%. The results revealed the significant effects of cobalt phosphide materials in

boosting H_2O_2 production. The optimal performance was obtained from Co_2P-modified BVO, whereas CoP was less effective. Compared with the reported results (**Table S1**), the performance in this work was significantly improved, and this result is mainly attributed to the loaded cobalt phosphide co-catalyst. During the reaction, O_2 gas, as the other product, can be simultaneously produced by four electron oxidation processes on the photoanode. The amount of generated O_2 gas was measured using gas chromatography. In addition, the stability of H_2O_2 production was evaluated in a continuous two-hour experiment, as shown in **Figure 3d**. During H_2O_2 synthesis, the formed species of $OH^{\bullet}$ and H_2O_2 are strong oxidants that can degrade the BVO film. In this study, the cobalt phosphide-modified photoanode (CPB-4) and pristine BVO exhibited a similar slow degradation of the photocurrent, suggesting that the degradation was caused by the oxidation of BVO rather than the Co_2P coating. Because it involves a higher concentration of H_2O_2 with the CPB-4 photoanode, this also suggests that the Co_2P coating inhibits the degradation of BVO. The stability of Co_2P was further confirmed by soaking Co_2P powder in a 0.01 M H_2O_2 solution for 36 h, and then probing by XRD (**Figure S7**). As a result, the spectra were generally preserved before and after the test, revealing that Co_2P was stable in the H_2O_2 solution.

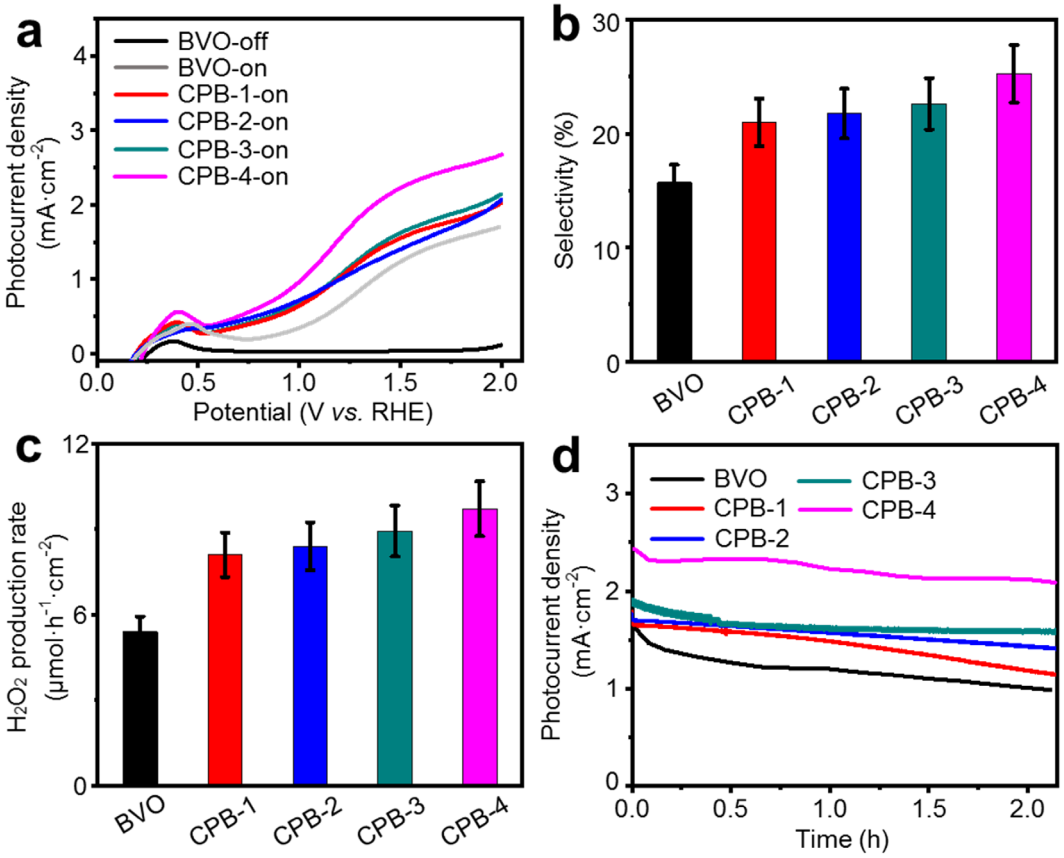

Figure 3. (a) LSV curve of photoanodic H_2O_2 production by the BVO and CPB photoanodes. (b) Selectivity, (c) the yield with three times of independent repeated experiments and (d) two-hour evolution of the H_2O_2 production by BVO and CPB photoanodes at 1.7 V_{RHE} under the illumination of a sunlight simulator.

Because the surface of the cobalt phosphides was easily oxidized, as demonstrated by the XPS results, Co_3O_4 particles were synthesized as a reference co-catalyst for photoanodic H_2O_2 production (**Figure S8**). Under the same reaction conditions, the yield and selectivity for H_2O_2 production were 6.6 $\mu mol \cdot h^{-1} \cdot cm^{-2}$ and 20%, respectively. Although the performance was better than that of the pristine BVO photoanode, it was lower than that of all CPB photoanodes. Hence, both Co and P played important roles in promoting the production of H_2O_2 with synergistic effects. The details of the functions of Co and P are discussed below.

3.4 Role of the cobalt phosphide on photoanodes for H_2O_2 production reaction

The light-absorption spectra of the BVO and CPB photoanodes are shown in **Figure 4a**. The absorption of BVO is generally preserved by loading cobalt phosphides because the low quantity of loaded cobalt phosphides (3 μg/cm^2) has an insignificant effect on the absorption spectrum. This suggests that the loading of cobalt phosphides does not affect the light-absorption behavior of BVO. The bandgap energies were determined using the Kubelka–Munk plots shown in **Figure S9**. All the samples had similar bandgap energies of 2.50 eV. The conduction band minimum (0.15 eV was obtained from the Mott–Schottky plots of the EIS measurements (**Figure S10**). Together with the bandgap energy, the valence band edge (2.35 eV) and the completed band structure of the photoanode are thus determined. The deposition of cobalt phosphide nanoparticles did not significantly change the band structure and extinction coefficient of BVO, which is likely due to the low loading of cobalt phosphide and weak physical interaction between the cobalt phosphide and BVO substrate. The incident photon-to-electron conversion efficiency (IPCE) for H_2O_2 production was determined (**Figure 4b**). Although the light absorption of the CPB photoanodes was the same as that of the BVO photoanode, the quantum efficiency increased with the loading of cobalt phosphides. The IPCE results confirm that despite cobalt phosphides having little effect on the bandgap and light absorption efficiency of BVO, the performance for H_2O_2 production was significantly increased [46], which must be associated with changes in the reaction pathways on the BVO surface.

Room-temperature photoluminescence (PL) was used to study the steady-state

behavior of photoexcited charge carriers in the BVO and CPB photoanodes. By applying excitation light at 360 nm, the PL signal showed an emission peak at 500 nm (**Figure S11**). The addition of cobalt phosphide to the BVO surface considerably decreased the PL emission intensity. The time-resolved PL (TRPL) spectra in **Figure 4c** were acquired at the same excitation wavelength. The fitted decay time of charge collection on the BVO photoanode was 1.08 ns, which increased slightly to 1.39 ns for CPB-4. This extended charge lifetime is in good agreement with the reduced PL signal of the CPB photoanode and could positively contribute to the improved performance in water oxidation. However, such an improvement resulting from the improvement in charge separation will not significantly affect the H_2O_2 selectivity because the OER reaction will also be increased. Thus, this may not be the main mechanism for improved H_2O_2 production.

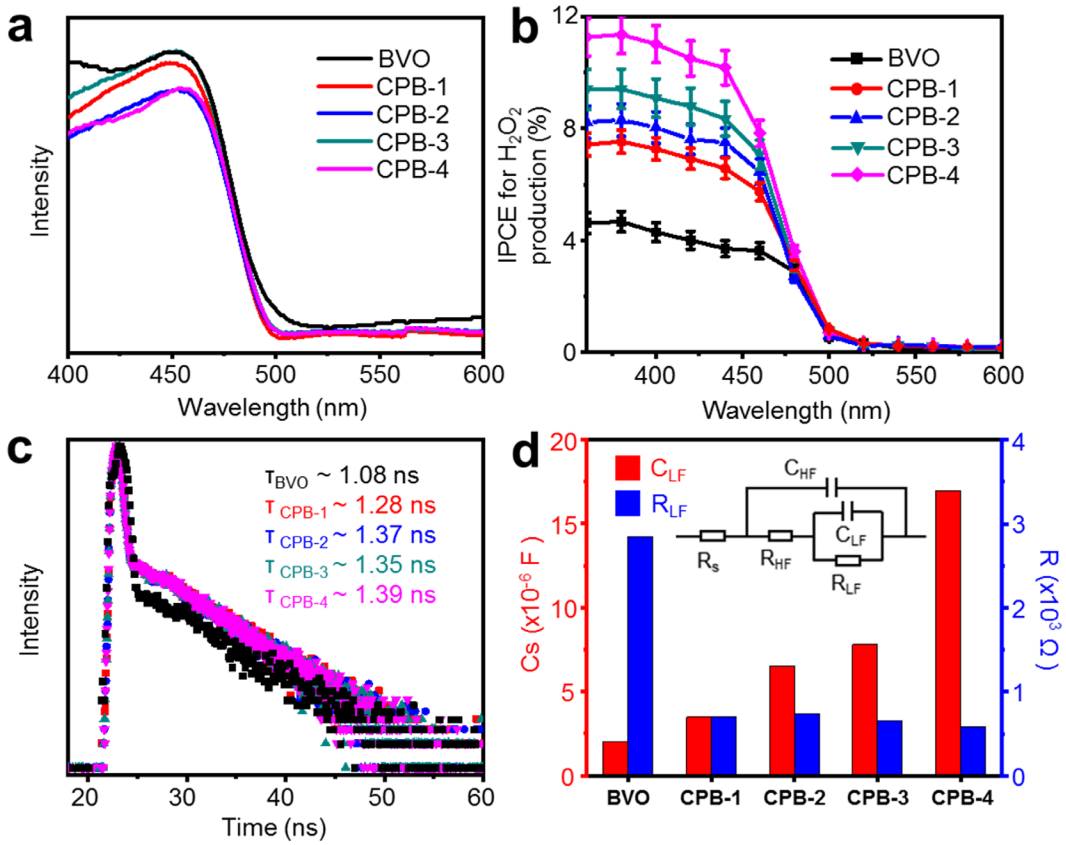

Figure 4. (a) UV-Vis DRS spectra, (b) IPCE plots with three times of independent repeated experiments (c) TRPL spectra of BVO and CPB photoanodes. (d) The analyses of the Nyquist plots of EIS using the equivalent circuit (inset).

Subsequently, EIS was conducted to study the charge accumulation in the CPB photoanodes. The Nyquist plot of EIS is presented in **Figure S12a,** and the analysis is shown in **Figure 4d** by fitting in an equivalent electrical circuit (inset of **Figure 4d**). Compared with the results achieved without light illumination (**Figure S12b** and **S12c**), the improvement is obvious. The high-frequency resistance (R_{HF}) is related to the resistance inside the bulk BVO. The high-frequency capacitance (C_{HF}) is related to charge accumulation at the interface between BVO and cobalt phosphide. The low-frequency resistance (R_{LF}) is related to the resistance of photoexcited charge transfer from the BVO films to the cobalt phosphide co-catalyst. The low-frequency capacitance

(C_{LF}) is associated with the charge accumulation capability of the photoanode. As shown in **Figure S12d**, the value of R_{HF} was evidently lower than that of R_{LF}. This is due to the faster charge transfer in bulk BVO, rather than crossing through the crystal surface of the two different materials. However, the value of C_{LF} is generally higher than that of C_{HF}. This indicates the better charge-accumulation ability of cobalt phosphide. The investigation of the surface of the photoanode is more important in this study. As shown in **Figure 4d**, the values of R_{LF} from CPB photoanodes are generally lower than those of BVO, indicating that the presence of cobalt phosphide improves charge transfer. However, this resistance was less sensitive to the Co:P ratio because there was no obvious difference between the different CPB photoanodes. This result agrees with the TRPL results. More importantly, the charge accumulation capability was significantly improved after the addition of the cobalt phosphide co-catalyst, especially by adding Co_2P nanoparticles.

The surface PEC reaction during H_2O_2 production was investigated with CV to establish the electrocatalytic redox process of cobalt phosphide. In this study, cobalt phosphide nanoparticles were loaded onto the FTO glass as an electrode, and the electrolyte solution was the same as that for photoanodic H_2O_2 production, i.e., 1.0 M $KHCO_3$ water solution. The scan was conducted ranging from 0.1 V to 1.9 V_{RHE} with a rate of 5 mV/s. For CoP, one anodic peak at 1.77 V_{RHE} was observed in **Figure 5b** for the first scanning cycle, corresponding to the oxidation of Co^{3+} to Co^{4+}. The oxidation peak from the second cycle became less detectable, probably because most of the Co^{3+} was oxidized to Co^{4+}, similar to that for the third cycle. In comparison, two anodic

peaks were identified for Co_2P at 1.53 and 1.75 V_{RHE} for the first scanning cycle, as shown in **Figure 5a**, corresponding to the redox couples of Co^{2+}/Co^{3+} and Co^{3+}/Co^{4+}, respectively [47, 48]. In the second scanning cycle, one peak was still observed at 1.75 V_{RHE}, which again confirms the redox couple of Co^{3+}/Co^{4+}. However, no obvious peak was observed from the third cycle. For the mixed-phase cobalt phosphides, two redox couples were also observed at 1.53 and 1.75 V_{RHE} (**Figure S13**), although the intensity of the peak at 1.53 V_{RHE} was weaker than that from Co_2P due to the lower population of Co^{2+} in the mixed-phase cobalt phosphides. The results indicate that, compared with CoP, Co_2P exhibited more valence states for charge accumulation for the electrochemical reaction, owing to the existence of Co^{2+}. Redox couples can be considered as active sites for the photocatalytic water oxidation reaction. Co_2P is likely to accumulate more photoexcited charges, thereby promoting H_2O_2 production. Thermodynamically, the charge accumulation property is reflected in the valence band potential relative to the water oxidation potential. Ultraviolet photoelectron spectroscopy (UPS) was used to determine the valence band of the cobalt phosphides (**Figure S14**) [49]. The potentials for different samples are shown in **Figure 5c**, which shows a gradually increasing valence potential with the CoP ratio. Hence, Co_2P is expected to provide the highest capacity for charge accumulation among the cobalt phosphides. The improved charge accumulation was directly correlated with H_2O_2 production.

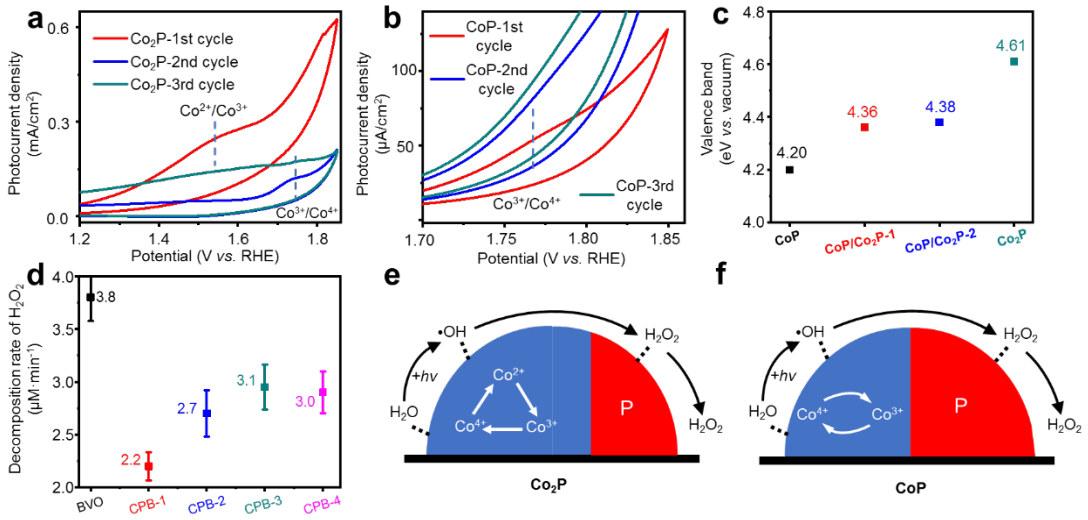

Figure 5. (a)-(b) CV curves of Co_2P and CoP. (c) The valence band of cobalt phosphide materials from UPS spectra. (d) H_2O_2 decomposition on BVO, CPB photoanodes for 1 h with three times of independent repeated experiments. (e) Illustration of the possible mechanism for H_2O_2 production on the surface of Co_2P and CoP.

The water oxidation reaction is restricted by the formation of $OH^{\bullet}$ radicals through the dissociation of one of the O-H bonds in H_2O. In this study, the formation of $OH^{\bullet}$ radicals were probed using an electron paramagnetic resonance spectrometer (EPR) under light illumination. The $OH^{\bullet}$ radicals reacted with 5,5-dimethyl-1-pyrroline N-oxide (DMPO) to exhibit quartet peaks with an intensity ratio of 1:2:2:1. As shown in **Figure S15**, this group of quartet peaks is observed for all photoanodes. However, the EPR intensities from the CPB photoanodes were generally higher than those from the BVO photoanode, with the highest intensity obtained from CPB-4, corresponding to the highest production rate of $OH^{\bullet}$ radicals. This result correlates with the highest production yield of H_2O_2 from the CPB-4 photoanode.

The produced $OH^{\bullet}$ radicals would subsequently couple to form H_2O_2 before desorption from the photoelectrode surfaces. If H_2O_2 desorption is slow, it could be

further oxidized to O_2 gas. Therefore, H_2O_2 desorption is important to the yield and selectivity of H_2O_2. A certain amount of H_2O_2 was added to the electrolyte solution to determine the desorption rate. Pristine BVO, CPB, and Co_3O_4-BVO photoanodes were placed in the electrolyte solution, and the reduction in H_2O_2 concentration in the electrolyte was measured as a function of time, as shown in **Figure S16**. This reduction in H_2O_2 concentration in the electrolyte was due to the adsorption of H_2O_2. A slower adsorption rate was associated with faster desorption. The pristine BVO photoanode exhibited the fastest H_2O_2 adsorption rate, suggesting the slowest desorption. With the addition of cobalt phosphides, the H_2O_2 adsorption rate decreased according to the P:Co ratio, as shown in the inset of **Figure 5d**. From the CPB photoanodes, the desorption rate follows the order CPB-1>CPB-2>CPB-3≈CPB-4, implying that the P site plays a key role in this desorption because the highest desorption rate was achieved from CPB-1 with the highest P:Co ratio.

The role of cobalt phosphide in highly efficient, selective H_2O_2 production is shown in **Figures 5e** and **5f**. The Co site is catalytically effective in dissociating one of the H-O bonds in H_2O to form $OH^{\bullet}$ radicals. In this process, the improved photoexcited charge accumulation promotes the formation of $OH^{\bullet}$ radicals. Therefore, among the cobalt phosphide materials, Co_2P with a high Co content exhibits the best performance owing to its high valence potential for accumulating photoexcited charges, as illustrated in **Figure 5e**. In contrast, the P species influence the desorption of the produced H_2O_2. The CoP with high P content therefore exhibits the optimum performance for the desorption of H_2O_2. The corresponding mechanism is illustrated in **Figure 5f**. Because

the difference in the H_2O_2 desorption rate of different cobalt phosphides is moderate, the conversion performance is mainly determined by the formation of $OH^{\bullet}$ radicals. Hence, Co_2P has the best H_2O_2 production performance as a co-catalyst for BVO.

4. Conclusions

In conclusion, cobalt phosphides have been developed as con-catalysts on the BVO photoanode to improve the performance of H_2O_2 production, including pristine CoP and Co_2P crystals and two mixed-phase cobalt phosphide (CoP/Co_2P) crystals. Among them, Co_2P exhibits optimal performance for H_2O_2 production; the optimal yield and selectivity are 9.6 $\mu mol \cdot h^{-1} \cdot cm^{-2}$ and 25.2%, respectively, at the voltage bias of 1.7 V_{RHE} under artificial sunlight illumination. The primary roles of the Co and P sites have been investigated as co-catalysts for H_2O_2 production. In particular, the Co site promotes the breaking of one H-O bond in water to form $OH^{\bullet}$ radicals, which is the rate-determining step in H_2O_2 production [50]. The P site plays an important role in the desorption of H_2O_2 formed from the catalyst [51], which is responsible for the recovery of fresh catalytic sites. This study reveals the synergistic mechanism of cobalt phosphide-based co-catalysts on a photoanode for H_2O_2 production and inspires a variety of applications, not only for solar conversion devices, but also for sensors, catalysis, and many others [52-57].

Credit authorship contribution statement

Yuntao Xu: Investigation, Methodology, Formal analysis, Data curation, and Writing–original draft. **Yanfei Cao**: Formal analysis, and Data curation. **Li Tan**: Investigation,

and Writing–original draft. **Qiao Chen**: Investigation, and Writing–original draft. **Yuanxing Fang**: Conceptualization, Methodology, Formal analysis, Investigation, Resources, Writing – review & editing, Visualization, Supervision, Project administration, and Funding acquisition.

Acknowledgments

This work was supported by the National Key R&D Program of China (2022YFE0114800), the National Natural Science Foundation of China (22075047), and the National Natural Science Foundation of Fujian Province of China (2020J01446).

References

[1] N. Agarwal, S.J. Freakley, R.U. McVicker, S.M. Althahban, N. Dimitratos, Q. He, D.J. Morgan, R.L. Jenkins, D.J. Willock, S.H. Taylor, C.J. Kiely, G.J. Hutchings, Aqueous Au-Pd colloids catalyze selective CH_4 oxidation to CH_3OH with O_2 under mild conditions, Science 358 (2017) 223-227.

[2] M. Yamada, K.D. Karlin, S. Fukuzumi, One-step selective hydroxylation of benzene to phenol with hydrogen peroxide catalysed by copper complexes incorporated into mesoporous silica–alumina, Chem. Sci. 7 (2016) 2856-2863.

[3] Y. Shi, Y. Xia, G. Xu, L. Wen, G. Gao, B. Zong, Hydrogen peroxide and applications in green hydrocarbon nitridation and oxidation, Chinese J. Chem. Eng. 41 (2022) 145-161.

[4] K. Dong, J. Liang, Y. Ren, Y. Wang, Z. Xu, L. Yue, T. Li, Q. Liu, Y. Luo, Y. Liu, S. Gao, M.S. Hamdy, Q. Li, D. Ma, X. Sun, Electrochemical two-electron O2 reduction reaction toward H2O2 production: using cobalt porphyrin decorated carbon nanotubes as a nanohybrid catalyst, J. Mater. Chem. A 9 (2021) 26019-26027.

[5] K. Dong, Z. Xu, X. He, D. Zhao, H. Chen, J. Liang, Y. Luo, S. Sun, D. Zheng, Q. Liu, A.A. Alshehri, Z. Feng, Y. Wang, X. Sun, Ultrathin single-crystal $PtSe_2$ nanosheets for high-efficiency O_2 electroreduction to H_2O_2, Chem. Commun. 58 (2022) 10683-10686.

[6] Q. Chen, C. Ma, S. Yan, J. Liang, K. Dong, Y. Luo, Q. Liu, T. Li, Y. Wang, L. Yue, B. Zheng, Y. Liu, S. Gao, Z. Jiang, W. Li, X. Sun, Greatly Facilitated Two-Electron Electroreduction of Oxygen into Hydrogen Peroxide over TiO_2 by Mn Doping, ACS Appl. Mater. Interfaces 13 (2021) 46659-46664.

[7] Z. Teng, Q. Zhang, H. Yang, K. Kato, W. Yang, Y.-R. Lu, S. Liu, C. Wang, A. Yamakata, C. Su, B. Liu, T. Ohno, Atomically dispersed antimony on carbon nitride for the artificial photosynthesis of hydrogen peroxide, Nat. Catal. 4 (2021) 374-384.

[8] X. Li, X. Chen, Y. Fang, W. Lin, Y. Hou, M. Anpo, X. Fu, X. Wang, High-performance potassium poly(heptazine imide) films for photoelectrochemical water splitting, Chem. Sci. 13 (2022) 7541-7551.

[9] R.S. Sprick, Z. Chen, A.J. Cowan, Y. Bai, C.M. Aitchison, Y. Fang, M.A. Zwijnenburg, A.I. Cooper, X. Wang, Water Oxidation with Cobalt-Loaded Linear

Conjugated Polymer Photocatalysts, Angew. Chem., Int. Ed. 59 (2020) 18695-18700.

[10] S.R. Kelly, X. Shi, S. Back, L. Vallez, S.Y. Park, S. Siahrostami, X. Zheng, J.K. Nørskov, ZnO As an Active and Selective Catalyst for Electrochemical Water Oxidation to Hydrogen Peroxide, ACS Catal. 9 (2019) 4593-4599.

[11] K. Wenderich, W. Kwak, A. Grimm, G.J. Kramer, G. Mul, B. Mei, Industrial feasibility of anodic hydrogen peroxide production through photoelectrochemical water splitting: a techno-economic analysis, Sustain. Energ. Fuels 4 (2020) 3143-3156.

[12] S. Hu, Membrane-less photoelectrochemical devices for H_2O_2 production: efficiency limit and operational constraint, Sustain. Energ. Fuels 3 (2019) 101-114.

[13] S. Naik Shreyanka, J. Theerthagiri, S.J. Lee, Y. Yu, M.Y. Choi, Multiscale design of 3D metal–organic frameworks (M−BTC, M: Cu, Co, Ni) via PLAL enabling bifunctional electrocatalysts for robust overall water splitting, Chem. Eng. J. 446 (2022) 137045.

[14] L. Wang, Y. Kong, Y. Fang, P. Cai, W. Lin, X. Wang, A Ga Doped $NiTiO_3$ Photocatalyst for Overall Water Splitting under Visible Light Illumination, Adv. Funct. Mater. 32 (2022) 2208101.

[15] Y. Fang, Y. Xu, X. Li, Y. Ma, X. Wang, Coating Polymeric Carbon Nitride Photoanodes on Conductive Y:ZnO Nanorod Arrays for Overall Water Splitting, Angew. Chem., Int. Ed. 57 (2018) 9749-9753.

[16] X. Li, J. Wang, J. Xia, Y. Fang, Y. Hou, X. Fu, M. Shalom, X. Wang, One-Pot Synthesis of CoS_2 Merged in Polymeric Carbon Nitride Films for Photoelectrochemical Water Splitting, Chemsuschem 15 (2022) e202200330.

[17] F. Hasché, M. Oezaslan, P. Strasser, T.-P. Fellinger, Electrocatalytic hydrogen peroxide formation on mesoporous non-metal nitrogen-doped carbon catalyst, J. Energy Chem. 25 (2016) 251-257.

[18] X. Shi, S. Siahrostami, G.-L. Li, Y. Zhang, P. Chakthranont, F. Studt, T.F. Jaramillo, X. Zheng, J.K. Nørskov, Understanding activity trends in electrochemical water oxidation to form hydrogen peroxide, Nat. Commun. 8 (2017) 701.

[19] L. Ji, Y. Wei, P. Wu, M. Xu, T. Wang, S. Wang, Q. Liang, T.J. Meyer, Z. Chen, Heterointerface Engineering of Ni_2P–Co_2P Nanoframes for Efficient Water Splitting, Chem. Mater. 33 (2021) 9165-9173.

[20] Y. Fang, X. Li, X. Wang, Phosphorylation of Polymeric Carbon Nitride Photoanodes with Increased Surface Valence Electrons for Solar Water Splitting, ChemSusChem 12 (2019) 2605-2608.

[21] J. Zhang, X. Chang, Z. Luo, T. Wang, J. Gong, A highly efficient photoelectrochemical H_2O_2 production reaction with Co_3O_4 as a co-catalyst, Chem. Commun. 54 (2018) 7026-7029.

[22] K. Mase, M. Yoneda, Y. Yamada, S. Fukuzumi, Efficient Photocatalytic Production of Hydrogen Peroxide from Water and Dioxygen with Bismuth Vanadate and a

Cobalt(II) Chlorin Complex, ACS Energy Lett. 1 (2016) 913-919.

[23] T.H. Jeon, H. Kim, H.-i. Kim, W. Choi, Highly durable photoelectrochemical H_2O_2 production via dual photoanode and cathode processes under solar simulating and external bias-free conditions, Energy Environ. Sci. 13 (2020) 1730-1742.

[24] L. Yang, H. Chen, Y. Xu, R. Qian, Q. Chen, Y. Fang, Synergetic effects by Co^{2+} and PO_4^{3-} on Mo-doped $BiVO_4$ for an improved photoanodic H_2O_2 evolution, Chem. Eng. Sci. 251 (2022) 117435.

[25] Y. Peng, L. Zhou, L. Wang, J. Lei, Y. Liu, S. Daniele, J. Zhang, Preparation of NiCoP-decorated g-C_3N_4 as an efficient photocatalyst for H_2O_2 production, Res. Chem. Intermediat. 45 (2019) 5907-5917.

[26] H. Kim, J. Lim, S. Lee, H.-H. Kim, C. Lee, J. Lee, W. Choi, Spontaneous Generation of H_2O_2 and Hydroxyl Radical through O_2 Reduction on Copper Phosphide under Ambient Aqueous Condition, Environ. Sci. Technol. 53 (2019) 2918-2925.

[27] Y. Guo, P. Yuan, J. Zhang, H. Xia, F. Cheng, M. Zhou, J. Li, Y. Qiao, S. Mu, Q. Xu, Co_2P–CoN Double Active Centers Confined in N-Doped Carbon Nanotube: Heterostructural Engineering for Trifunctional Catalysis toward HER, ORR, OER, and Zn–Air Batteries Driven Water Splitting, Adv. Funct. Mater. 28 (2018) 1805641.

[28] J. Theerthagiri, K. Karuppasamy, S.J. Lee, R. Shwetharani, H.-S. Kim, S.K.K. Pasha, M. Ashokkumar, M.Y. Choi, Fundamentals and comprehensive insights on pulsed laser synthesis of advanced materials for diverse photo- and electrocatalytic

applications, Light-Sci. Appl. 11 (2022) 250.

[29] T.R. Hellstern, J.D. Benck, J. Kibsgaard, C. Hahn, T.F. Jaramillo, Engineering Cobalt Phosphide (CoP) Thin Film Catalysts for Enhanced Hydrogen Evolution Activity on Silicon Photocathodes, Adv. Energy Mater. 6 (2016) 1501758.

[30] L.A. King, M.A. Hubert, C. Capuano, J. Manco, N. Danilovic, E. Valle, T.R. Hellstern, K. Ayers, T.F. Jaramillo, A non-precious metal hydrogen catalyst in a commercial polymer electrolyte membrane electrolyser, Nat. Nanotechnol. 14 (2019) 1071-1074.

[31] T.W. Kim, K.-S. Choi, Nanoporous $BiVO_4$ Photoanodes with Dual-Layer Oxygen Evolution Catalysts for Solar Water Splitting, Science 343 (2014) 990-994.

[32] L. Liao, C. Cheng, H. Zhou, Y. Qi, D. Li, F. Cai, B. Yu, R. Long, F. Yu, Accelerating pH-universal hydrogen-evolving activity of a hierarchical hybrid of cobalt and dinickel phosphides by interfacial chemical bonds, Mater. Today Phys. 22 (2022) 100589.

[33] X. Shi, Y. Zhang, S. Siahrostami, X. Zheng, Light-Driven $BiVO_4$–C Fuel Cell with Simultaneous Production of H_2O_2, Adv. Energy Mater. 8 (2018) 1801158.

[34] S.S. Naik, S.J. Lee, J. Theerthagiri, Y. Yu, M.Y. Choi, Rapid and highly selective electrochemical sensor based on ZnS/Au-decorated f-multi-walled carbon nanotube nanocomposites produced via pulsed laser technique for detection of toxic nitro compounds, J. Hazard. Mater. 418 (2021) 126269.

[35] K. Fuku, Y. Miyase, Y. Miseki, T. Gunji, K. Sayama, Enhanced Oxidative Hydrogen Peroxide Production on Conducting Glass Anodes Modified with Metal Oxides, ChemistrySelect 1 (2016) 5721-5726.

[36] K. Fuku, K. Sayama, Efficient oxidative hydrogen peroxide production and accumulation in photoelectrochemical water splitting using a tungsten trioxide/bismuth vanadate photoanode, Chem. Commun. 52 (2016) 5406-5409.

[37] L. Wang, P. Cai, Z. Liu, Z. Xie, Y. Fang, Role of carbon quantum dots on Nickel titanate to promote water oxidation reaction under visible light illumination, J. Colloid Interf. Sci. 607 (2022) 203-209.

[38] C. Ampelli, F. Tavella, C. Genovese, S. Perathoner, M. Favaro, G. Centi, Analysis of the factors controlling performances of Au-modified TiO_2 nanotube array based photoanode in photo-electrocatalytic (PECa) cells, J. Energy Chem. 26 (2017) 284-294.

[39] Y. Fang, I.S. Merenkov, X. Li, J. Xu, S. Lin, M.L. Kosinova, X. Wang, Vertically aligned 2D carbon doped boron nitride nanofilms for photoelectrochemical water oxidation, J. Mater. Chem. A 8 (2020) 13059-13064.

[40] D.R. Baer, Y.-C. Wang, D.G. Castner, Use of XPS to Quantify Thickness of Coatings on Nanoparticles, Microscopy Today 24 (2016) 40-45.

[41] M.M. Alsabban, M.K. Eswaran, K. Peramaiah, W. Wahyudi, X. Yang, V. Ramalingam, M.N. Hedhili, X. Miao, U. Schwingenschlogl, L.J. Li, V. Tung, K.W. Huang, Unusual Activity of Rationally Designed Cobalt Phosphide/Oxide

Heterostructure Composite for Hydrogen Production in Alkaline Medium, ACS Nano 16 (2022) 3906-3916.

[42] A.P. Grosvenor, S.D. Wik, R.G. Cavell, A. Mar, Examination of the Bonding in Binary Transition-Metal Monophosphides MP (M = Cr, Mn, Fe, Co) by X-Ray Photoelectron Spectroscopy, Inorg. Chem. 44 (2005) 8988-8998.

[43] P.E.R. Blanchard, A.P. Grosvenor, R.G. Cavell, A. Mar, X-ray Photoelectron and Absorption Spectroscopy of Metal-Rich Phosphides M2P and M3P (M = Cr−Ni), Chem. Mater. 20 (2008) 7081-7088.

[44] S. Liu, W. Wang, Y. Cheng, L. Yao, Y. Liu, M. Lin, H. Chen, Y. Liang, J. Fu, L. Wang, Design and fabrication of ternary $BiVO_4/FeVO_4/Cu_2O$ nanorod array photoelectrode for boosting photoelectrochemical water oxidation, Ceram. Int. 48 (2022) 7613-7621.

[45] Y. Yu, S.S. Naik, Y. Oh, J. Theerthagiri, S.J. Lee, M.Y. Choi, Lignin-mediated green synthesis of functionalized gold nanoparticles via pulsed laser technique for selective colorimetric detection of lead ions in aqueous media, J. Hazard. Mater. 420 (2021) 126585.

[46] P. Tan, A. Zhu, Y. Liu, Y. Ma, W. Liu, H. Cui, J. Pan, Insights into the efficient charge separation and transfer efficiency of La,Cr-codoped $SrTiO_3$ modified with CoP as a noble-metal-free co-catalyst for superior visible-light driven photocatalytic hydrogen generation, Inogr. Chem. Front. 5 (2018) 679-686.

[47] X. Chen, M. Cheng, D. Chen, R. Wang, Shape-Controlled Synthesis of Co_2P Nanostructures and Their Application in Supercapacitors, ACS Appl. Mater. Interfaces 8 (2016) 3892-3900.

[48] W. Peng, L. Jiao, Q. Huan, L. Li, J. Yang, Q. Zhao, Q. Wang, H. Du, G. Liu, Y. Si, Y. Wang, H. Yuan, Co_2P: A facile solid state synthesis and its applications in alkaline rechargeable batteries, J. Alloy. Compd. 511 (2012) 198-201.

[49] A. Sharma, R. Berger, D.A. Lewis, G.G. Andersson, Invisible high workfunction materials on heterogeneous surfaces, Appl. Surf. Sci. 327 (2015) 22-26.

[50] P. Zhang, T. Wang, X. Chang, L. Zhang, J. Gong, Synergistic Cocatalytic Effect of Carbon Nanodots and Co_3O_4 Nanoclusters for the Photoelectrochemical Water Oxidation on Hematite, Angew. Chem., Int. Ed. 55 (2016) 5851-5855.

[51] G.-h. Moon, W. Kim, A.D. Bokare, N.-e. Sung, W. Choi, Solar production of H_2O_2 on reduced graphene oxide–TiO_2 hybrid photocatalysts consisting of earth-abundant elements only, Energ. Environ. Sci. 7 (2014) 4023-4028.

[52] Y. Gao, Y. Zeng, X. Liu, D. Tang, Liposome-Mediated In Situ Formation of Type-I Heterojunction for Amplified Photoelectrochemical Immunoassay, Anal. Chem. 94 (2022) 4859-4865.

[53] Z. Yu, H. Gong, J. Xu, Y. Li, Y. Zeng, X. Liu, D. Tang, Exploiting Photoelectric Activities and Piezoelectric Properties of $NaNbO_3$ Semiconductors for Point-of-Care Immunoassay, Anal. Chem. 94 (2022) 3418-3426.

[54] S. Lv, K. Zhang, Y. Zeng, D. Tang, Double Photosystems-Based 'Z-Scheme' Photoelectrochemical Sensing Mode for Ultrasensitive Detection of Disease Biomarker Accompanying Three-Dimensional DNA Walker, Anal. Chem. 90 (2018) 7086-7093.

[55] J. Shu, Z. Qiu, Z. Lin, G. Cai, H. Yang, D. Tang, Semiautomated Support Photoelectrochemical Immunosensing Platform for Portable and High-Throughput Immunoassay Based on Au Nanocrystal Decorated Specific Crystal Facets $BiVO_4$ Photoanode, Anal. Chem. 88 (2016) 12539-12546.

[56] S. Yang, A. Verdaguer-Casadevall, L. Arnarson, L. Silvioli, V. Čolić, R. Frydendal, J. Rossmeisl, I. Chorkendorff, I.E.L. Stephens, Toward the Decentralized Electrochemical Production of H_2O_2: A Focus on the Catalysis, ACS Catal. 8 (2018) 4064-4081.

[57] Z. Deng, L. Li, Y. Ren, C. Ma, J. Liang, K. Dong, Q. Liu, Y. Luo, T. Li, B. Tang, Y. Liu, S. Gao, A.M. Asiri, S. Yan, X. Sun, Highly efficient two-electron electroreduction of oxygen into hydrogen peroxide over Cu-doped TiO_2, Nano. Res. 15 (2022) 3880-3885.